

Research



Cite this article: Ware MR, Glownia JM, Natan A, Cryan JP, Bucksbaum PH. 2019 On the limits of observing motion in time-resolved X-ray scattering. *Phil. Trans. R. Soc. A* **377**: 20170477.
<http://dx.doi.org/10.1098/rsta.2017.0477>

Accepted: 12 November 2018

One contribution of 15 to a theme issue 'Measurement of ultrafast electronic and structural dynamics with X-rays'.

Subject Areas:

atomic and molecular physics, chemical physics, optics

Keywords:

time-resolved X-ray scattering, molecular movies, X-ray free electron lasers

Author for correspondence:

Matthew R. Ware
e-mail: mrware@stanford.edu

Electronic supplementary material is available online at <https://dx.doi.org/10.6084/m9.figshare.c.4409558>.

On the limits of observing
motion in time-resolved X-ray
scattering

Matthew R. Ware^{1,2}, James M. Glownia⁴, Adi Natan¹,
James P. Cryan^{1,4} and Philip H. Bucksbaum^{1,2,3}

¹National Accelerator Laboratory, Stanford PULSE Institute, Menlo Park, CA 94025, USA

²Department of Physics, and ³Department of Applied Physics, Stanford University, Stanford, CA 94305, USA

⁴National Accelerator Laboratory, LCLS, SLAC, Menlo Park, CA 94025, USA

JMG, 0000-0002-6172-7946; JPC, 0000-0002-7776-0919

Limits on the ability of time-resolved X-ray scattering (TRXS) to observe harmonic motion of amplitude, A and frequency, ω_0 , about an equilibrium position, R_0 , are considered. Experimental results from a TRXS experiment at the LINAC Coherent Light Source are compared to classical and quantum theories that demonstrate a fundamental limitation on the ability to observe the amplitude of motion. These comparisons demonstrate dual limits on the spatial resolution through Q_{\max} and the temporal resolution through ω_{\max} for observing the amplitude of motion. In the limit where $\omega_{\max} \approx \omega_0$, the smallest observable amplitude of motion is $A = 2\pi/Q_{\max}$. In the limit where $\omega_{\max} \geq 2\omega_0$, $A \leq 2\pi/Q_{\max}$ is observable provided there are sufficient statistics.

This article is part of the theme issue 'Measurement of ultrafast electronic and structural dynamics with X-rays'.

1. Introduction

Time-resolved X-ray and electron scattering (TRXS and TRES) have the potential to track nuclear and even electronic motion in molecules with atomic-level spatial and temporal resolution [1–3]. In TRXS experiments, the common current practice is to acquire nuclear positions

by fitting scattering data to a theoretical model [4–6]. This reliance on theory presents a challenge when working to interpret published experimental data. For example, a model fit might resolve periodic motion with an amplitude of 0.005 \AA in an experiment with 1.8 \AA of diffraction limited resolution [6]. When is such a result statistically valid? Nuclear positions can also be obtained via *de novo* methods, i.e. by directly inverting the time-dependent X-ray scattering measured in momentum space into real space [2,3,7–9]. These methods raise additional questions. For example, the signal-to-noise ratio of an experiment can limit the fidelity of reconstructed nuclear positions, and incomplete information in the X-ray scattering pattern can lead to artefacts in the reconstructed real-space movies of nuclear motion. When interpreting TRXS results using these two approaches, we require a rule analogous to the diffraction limit for static imaging ($d \geq 2\pi/Q_{\text{max}}$) to determine if a result is reasonable or significant. Some prior work has been done to place limits on the ability of TRXS to resolve motion. For example, Budarz *et al.* [4] discuss the blurring of the scattering pattern due to the finite scattering length of the sample cell, and Kirrander & Weber [10] discuss the limited resolution that arises due to the nature of the excited molecular wavepacket as opposed to the limitations of TRXS itself. Here we investigate the physical limits imposed by the measurement method itself. The goal is to establish criteria for the resolving power of TRXS to measure periodic motion with amplitude, A , about an equilibrium position, R_0 .

2. Experiment and theory

The experiments under consideration are scattering from homonuclear diatomic molecules in the gas phase. Photoexcitation of molecular iodine, I_2 , is a particular focus for which we have collected data to compare with our findings. Perhaps the simplest motion that we can study is the coherent oscillation of molecular iodine in its ground electronic state following Raman excitation with 800 nm light as shown in figure 1. The ground state of I_2 has been well-characterized by spectroscopy to have an equilibrium separation of 2.666 \AA and a harmonic period of 155.5 fs [11–13], and pump-probe spectroscopies have directly observed vibrational wavepackets on the ground state [14]. We have studied the ground state motion of molecular iodine in the gas phase using the TRXS apparatus depicted in figure 2. The 800 nm pump pulse induces coherent motion ($\Delta v \pm 1$ [15]) of the individual iodine molecules, then the X-ray probe pulse arrives at variable delay, $\tau = t - t_0$, and scatters onto the two-dimensional (x, y) detector as shown schematically in figure 3 and discussed in detail in appendix A. In any TRXS experiment, the direct observable is the delay-dependent scattered X-ray intensity, $I(x, y, \tau)$, on the two-dimensional detector as shown in figure 4. The molecular scattering factor, $S(x, y, \tau)$, is extracted from $I(x, y, \tau)$ as described in appendix B. $S(x, y, \tau)$ is the key observable for determining interatomic distances in a TRXS experiment. To obtain interatomic distances, the pixel coordinates (x, y) at the detector must be mapped onto the momentum transfer, $Q = k_0 - k_s$, which is done using the scattering angle, γ , shown in figure 3, to find $Q = 2k_0 \sin(\gamma/2)$. Here the molecular scattering factor is angularly integrated at Q to obtain the isotropic scattering factor, $S(Q, \tau)$.

The isotropic molecular scattering factor is related to the nuclear probability density, $\rho(R, \tau)$, through a spatial transform, i.e.

$$S(Q, \tau) = \int dR R^2 \text{sinc}(QR) \rho(R, \tau), \quad (2.1)$$

where R is the internuclear separation and τ is the delay between the optical-pump and X-ray-probe pulses.

The measured $S(Q, \tau)$ following the 800 nm pump pulse is shown in figure 5. Following some fast dissociation near t_0 , the dominant signal is a fast beat with a period of $155.9 \pm 3.9 \text{ fs}$. The beat period is consistent with the previously measured harmonic period of the ground state of iodine, 155.5 fs , from [11,12].

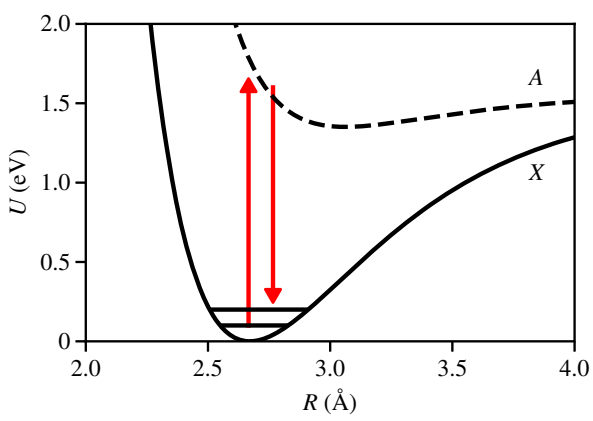


Figure 1. A strong 800 nm pump drives the Raman transition from and back onto the ground *X* state of iodine creating a vibrational wavepacket in the harmonic region of the *X* state. (Online version in colour.)

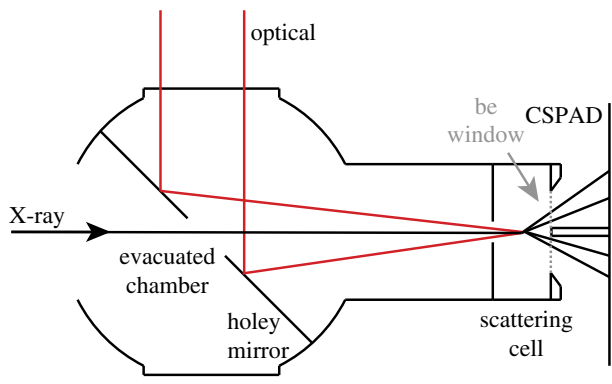


Figure 2. Within an evacuated chamber the incident X-ray pulse passes through a holey mirror. The optical pump reflects from the holey mirror and copropagates to the scattering cell alongside the X-ray pulse. The optical and X-ray pulses are focused onto the I_2 sample within the scattering cell. The X-rays scatter from the sample with an intensity profile which is sensitive to the delay between the optical pump pulse and the incident X-ray pulse. The scattered X-rays then travel freely to the Cornell Stanford Pixel Area Detector (CSPAD) through the output beryllium window. (Online version in colour.)

While $S(Q, \tau)$ is the starting point for de novo methods and may be directly inverted like

$$\rho(R, \tau) = \int dQ Q^2 \text{sinc}(QR) S(Q, \tau) \tag{2.2}$$

as shown in [9], the clear oscillations on the *X* state motivate an analysis of the temporal TRXS spectrum. Simple harmonic motion like $R(\tau) = R_0 + A \cos(\omega_0 \tau + \phi)$ may be leveraged to invert the scattering pattern by first taking a temporal Fourier transform of the measured scattering pattern, i.e.

$$\tilde{S}(Q, \omega) = \int_{-\infty}^{+\infty} d\tau e^{-i\omega\tau} S(Q, \tau). \tag{2.3}$$

From the measured TRXS, $S(Q, \tau)$, the harmonic motion of iodine in its ground state may be isolated by taking a temporal Fourier transform, $\tilde{S}(Q, \omega)$, as shown in figure 6. To gain insight into the TRXS spectrum at the harmonic frequency of 40.3 ± 1.0 THz, a classical model for $\tilde{S}(Q, \omega)$ using simple harmonic motion is now derived.

Classical isotropic time-resolved X-ray scattering may be expressed as

$$S(Q, t) = \text{sinc} QR(t), \tag{2.4}$$

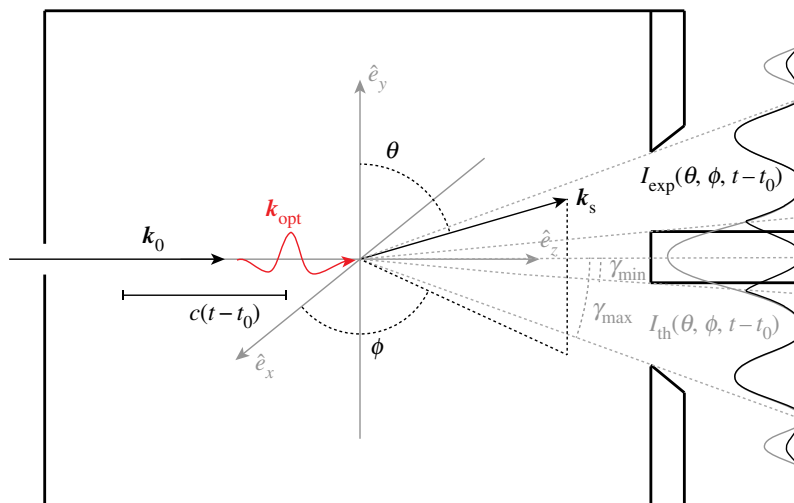


Figure 3. Sketch of the scattering cell and the scattering geometry of the experiment. γ_{min} and γ_{max} are the minimum and maximum scattering angles collected at the detector. Beyond γ_{min} and γ_{max} , the measured intensity is attenuated relative to the predicted intensity profile. (θ, ϕ) is the relevant angular decomposition about the laser polarization axis, \hat{e}_y , as the molecules align along this axis. \mathbf{k}_0 and \mathbf{k}_{opt} are the incident X-ray and optical wavevectors, respectively. Because the X-rays may scatter anywhere within the cell, the obtained scattering image is blurred by $\Delta\gamma = 3.4^\circ$ (i.e. 0.26 \AA^{-1} in Q -space), see [4]. (Online version in colour.)

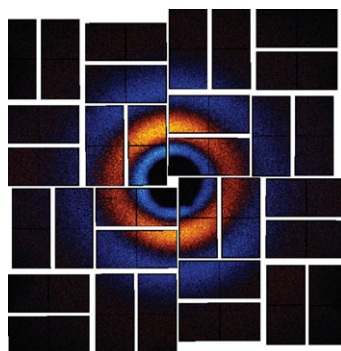


Figure 4. Difference image at the X-ray detector (CSPAD) for a delay of approximately 100 fs after pumping with 800 nm light.

from [16]. The above equation may be rewritten as

$$\begin{aligned}
 S(Q, t) &= \frac{1}{Q} \int_0^Q dQ' \cos(Q'R(t)) \\
 &= \frac{1}{2Q} \int_0^Q dQ' \left[e^{iQ'R(t)} + e^{-iQ'R(t)} \right] \\
 &= \frac{1}{2Q} (I_+ + I_-).
 \end{aligned} \tag{2.5}$$

Then,

$$\tilde{S}(Q, \omega) = \frac{1}{2Q} (\tilde{I}_+ + \tilde{I}_-), \tag{2.6}$$

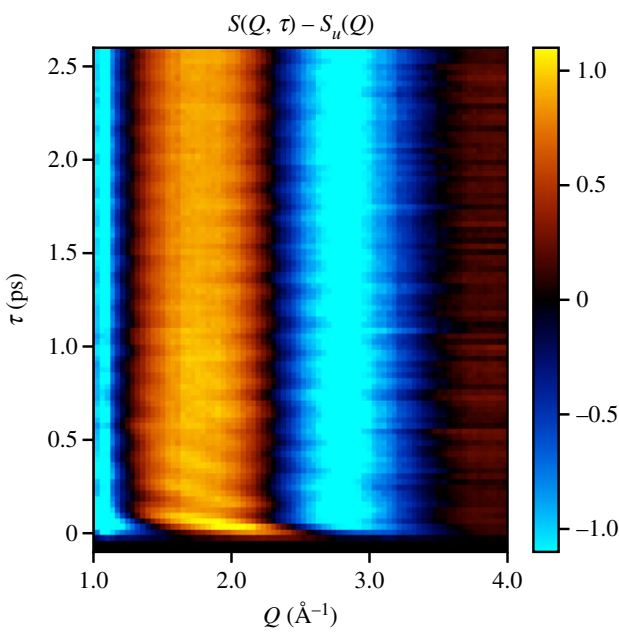


Figure 5. Time-resolved X-ray scattering following photoexcitation by an 800 nm pump pulse. This is the isotropic component of the molecular scattering factor. A fast 155.9 ± 3.9 fs beat is observed, corresponding to the harmonic period of the ground state of iodine. The unpumped scattering signal, $S_u(Q)$, is subtracted from this image.

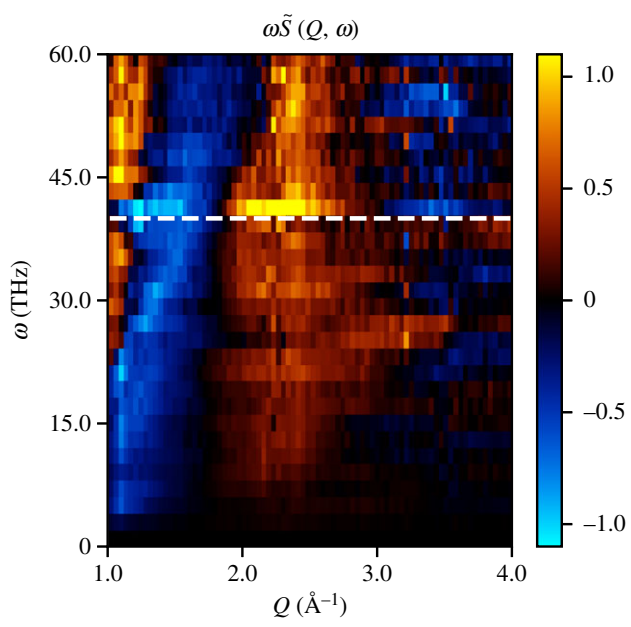


Figure 6. Temporal Fourier transform of figure 5. We observe a strong frequency component at 40.3 ± 1.0 THz corresponding to the harmonic frequency of the ground state of iodine. The lineout at this frequency may be used to obtain the equilibrium separation of the atoms in motion as shown in figure 7.

where

$$\tilde{I}_{\pm} = \frac{1}{2\pi} \int_0^Q dQ' \int_{-\infty}^{+\infty} dt e^{\pm iQ'R(t) - i\omega t}. \quad (2.7)$$

Laser initiated periodic motion may be expressed as a piece-wise function, where $R(t) = R_0$ for $t \leq t_0$ and $R(t) = R_0 + A \cos(\omega_0 t + \phi)$ for $t > t_0$. To obtain an analytic solution, the time-range of motion must be extended from (t_0, ∞) to $(-\infty, \infty)$. Using $R(t) = R_0 + A \cos(\omega_0 t + \phi)$ for $t \in (-\infty, \infty)$,

$$\tilde{I}_{\pm} = \frac{1}{2\pi} \int_0^Q dQ' e^{\pm iQ'R_0} \int_{-\infty}^{+\infty} dt e^{\pm iQ'A \cos(\omega_0 t + \phi) - i\omega t}. \quad (2.8)$$

In the limit $QA \ll 1$, the exponential expands to first order as

$$e^{\pm iQ'A \cos(\omega_0 t + \phi)} \approx 1 \pm iQ'A \cos(\omega_0 t + \phi). \quad (2.9)$$

Ignoring the addition of 1 as it only contributes to DC, equation (2.9) evaluates as follows:

$$\begin{aligned} \tilde{I}_{\pm} &\approx \frac{\pm iA}{4\pi} \int_0^Q dQ' Q' e^{\pm iQ'R_0} \int_{-\infty}^{+\infty} dt \left(e^{i\omega_0 t + i\phi - i\omega t} + e^{-i\omega_0 t - i\phi - i\omega t} \right) \\ &\approx \frac{\pm iA}{2} \int_0^Q dQ' Q' e^{\pm iQ'R_0} \left(e^{i\phi} \delta(\omega - \omega_0) + e^{-i\phi} \delta(\omega + \omega_0) \right) \\ &\approx \frac{\pm iA}{2} \left[-\frac{1}{R_0^2} + e^{\pm iQR_0} \left(\frac{1}{R_0^2} \mp \frac{iQ}{R_0} \right) \right] \left(e^{i\phi} \delta(\omega - \omega_0) + e^{-i\phi} \delta(\omega + \omega_0) \right), \end{aligned} \quad (2.10)$$

where $\cos(\omega_0 t + \phi)$ was expanded as an addition of exponentials and the definition for the Dirac delta function was used to solve the integral. The evaluation of \tilde{I}_{\pm} goes into equation (2.6) to find

$$\tilde{S}(Q, \omega = \pm\omega_0) = \frac{A}{2R_0} (\cos QR_0 - \text{sinc} QR_0), \quad (2.11)$$

where $\tilde{S}(Q, \omega)$ is zero for all other non-zero ω . The above equation is the classical model for $\tilde{S}(Q, \omega)$ from a diatomic undergoing simple harmonic motion.

Equation (2.11) has a notable feature. The amplitude of motion, A , does not contribute a spatial beat in $\tilde{S}(Q, \omega)$ for $A \ll 1/Q_{\max}$, and the prefactor $A/2R_0$ is indistinguishable from the overall excitation fraction of this state. This suggests that $Q_{\max} \geq 1/A$ is required to observe the amplitude of motion, and that experiments in the limit of low Q , i.e. $Q_{\max} \ll 1/A$, do not observe the amplitude of motion. To confirm the classical model, the discussion now returns to the experimental data.

For a Raman excitation, an amplitude of motion on the order of 0.2 \AA is anticipated within the harmonic region of the potential. This would require $Q_{\max} \geq 5 \text{ \AA}^{-1}$ to observe according to the classical model, so if the experiment is insensitive to the amplitude of motion, it should match the classical model. The classical model is compared to the measurement in figure 7. Between 1.81 and 4 \AA^{-1} , the model and measurement agree to within the experimental error. The statistical experimental error is calculated by finding the mean X-ray intensity, $I(x, y, \tau)$, at each pixel and across each pump-probe shot for that time-delay, and the variance of $I(x, y, \tau)$. This is then propagated through our analysis as described in appendix C. Below 1.81 \AA^{-1} , the signal is attenuated due to a physical beam block as shown in figure 3, and above 4 \AA^{-1} , the signal is not statistically significant due to few photon counts. This comparison supports the validity of the classical model and the existence of a limit on the ability to observe motion in a TRXS experiment analogous to the static limit of $d \geq 2\pi/Q_{\max}$. The comparison does not, however, inform us as to the Q_{\max} required to observe the amplitude of motion.

To investigate the required Q_{\max} , the quantum description for the nuclear probability density is now considered. Consider the nuclear probability density generated by the overlap of the two low lying vibrational states of iodine, ψ_v and ψ_{v+1} . These produce a charge density given by

$$\begin{aligned} \rho(R, \tau) &= \left| a\psi_v(R) e^{-iE_v\tau/\hbar} + b\psi_{v+1}(R) e^{-iE_{v+1}\tau/\hbar - i\phi} \right|^2 \\ &= a^2 |\psi_v(R)|^2 + b^2 |\psi_{v+1}(R)|^2 + 2ab \cos(\omega_0\tau + \phi) \psi_v \psi_{v+1}, \end{aligned} \quad (2.12)$$

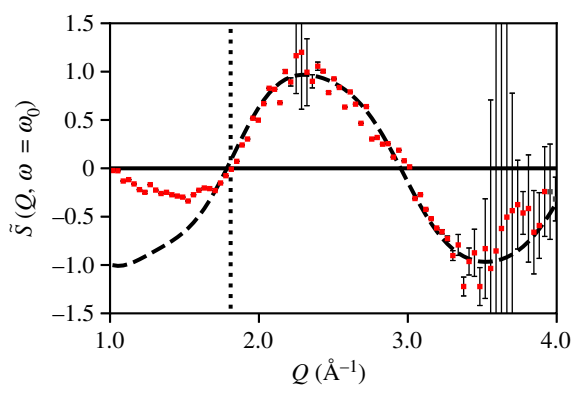


Figure 7. Lineout of figure 6 as compared to the classical theory for scattering from a vibrating diatomic. The error bars arise from a shot-by-shot statistical analysis and do not account for systematic effects. The statistical error increases at high Q where the measured intensity is low. Below the dashed line at 1.81\AA^{-1} , the signal is attenuated due to a physical beam block as shown in figure 3. (Online version in colour.)

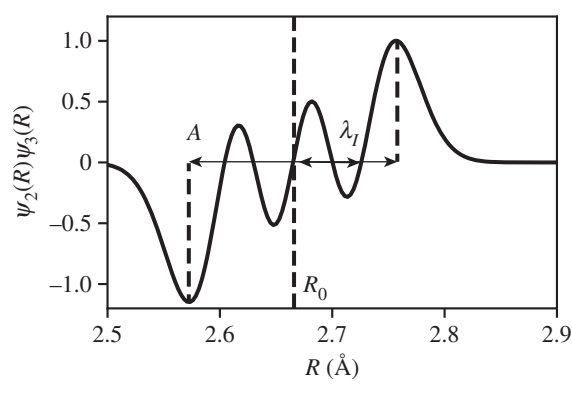


Figure 8. We show $\psi_v(R)\psi_{v+1}(R)$ using $v = 2$ and $v = 3$. There are three notable spatial features of this wave function: the central position R_0 , the amplitude of oscillation A and the wavelength between nodes, λ_j . Only R_0 impacts the structure of scattering at low Q as shown in figure 9. Note that $(v = 2, v + 1 = 3)$ are chosen for discussion not because they may be fingerprinted in the experimental data but because $\psi_2(R)\psi_3(R)$ clearly highlights the difference between A and λ_j .

where a^2 and b^2 are the excitation fractions, E_v and E_{v+1} are the eigenenergies, $\omega_0 = (E_{v+1} - E_v)/\hbar$, and ϕ is the relative phase of the states. Plugging equation (2.12) into equations (2.1) and (2.3), we find that

$$\tilde{S}(Q, \omega = \omega_0) = \int dRR^2 \text{sinc}(QR)\psi_v(R)\psi_{v+1}(R). \quad (2.13)$$

This shows that TRXS spectrum is simply the momentum-space transform of $\psi_v(R)\psi_{v+1}(R)$. (The coherent and incoherent contribution of different choices of v and $v + 1$ states, e.g. $(v = 1, v + 1 = 2)$ versus $(v = 2, v + 1 = 3)$, does not change the observed scattering at $Q < 5 \text{\AA}^{-1}$ as only R_0 impacts the scattering at low Q . Above this threshold, the interference of these terms is evident.)

Depending on the range of Q , $\tilde{S}(Q, \omega = \omega_0)$ may obtain information on the equilibrium position, the amplitude of oscillation, or the width of the distribution as shown in figure 8. We observe in figure 9 that the classical and the quantum results agree in the limit of $Q < 5 \text{\AA}^{-1}$, and we observe in figure 10 that the amplitude of motion is embedded in the high Q limit. In particular, we observe nodes at $Q = 2\pi/A$ and $Q = 4\pi/A$ for $A \approx 0.2 \text{\AA}$. Therefore, the analogy to the static limit, $d \geq 2\pi/Q_{\text{max}}$, for resolving harmonic motion of amplitude, A , is $A \geq 2\pi/Q_{\text{max}}$.

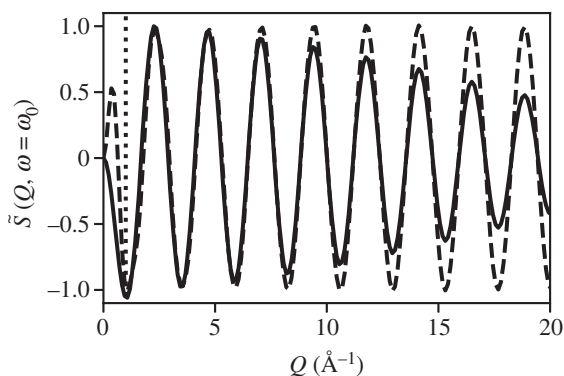


Figure 9. Comparison of the classical theory for $\tilde{S}(Q, \omega = \omega_0)$ (dashed line) and the quantum mechanical model for the same system (solid line). We observe that the classical model has an artefact below 1 \AA^{-1} due to the Dirac delta representation. Otherwise the two models agree up to about 7 \AA^{-1} at which point we begin to observe changes that can only be attributed to the amplitude of motion and fine structure of the wavepacket as shown in figure 10.

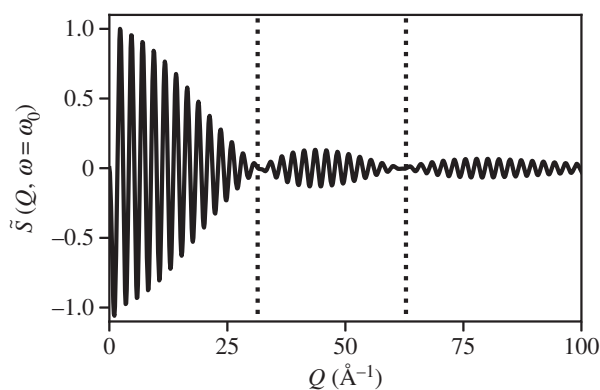


Figure 10. Extended range of $\tilde{S}(Q, \omega = \omega_0)$ for the wave function shown in figure 8. Nodes exist at $2\pi/A$ and $4\pi/A$, where $A \approx 0.2 \text{ \AA}$.

3. Discussion and conclusion

This does not rule out measuring an amplitude of $A \leq 2\pi/Q_{\max}$, but to do so requires observing higher multiples of the fundamental frequency. The classical theory suggests these are small in the limit $Q \ll 1/A$. The quantum theory shows that scattering from $\psi_{v-1}(R)\psi_{v+1}(R)$, i.e. the $2\omega_0$ signal, is no stronger than 25% of the $\psi_v(R)\psi_{v+1}(R)$ signal below 4 \AA^{-1} as shown in figure 11, and that is before accounting for the relative excitation fractions of the states which would only further reduce the relative signal. That said, there is evident impact of the amplitude of motion on the scattering at low Q for states $\psi_{v-1}(R)\psi_{v+1}(R)$, so with sufficient time-resolution and statistics even small oscillatory motions might be observable with TRXS.

This suggests that there are dual requirements on both ω_{\max} and Q_{\max} to observe the amplitude of oscillatory motion. For example, an experiment like the one described here with approximately 40 fs of temporal resolution measuring motion with a 155 fs period requires $Q_{\max} > 2\pi/A$ of resolution to measure the amplitude of motion. If instead the experiment had sufficient time resolution to measure the $2\omega_0$ beat, the amplitude of motion might have been resolvable with the $Q_{\max} = 4.0 \text{ \AA}^{-1}$ of the experiment. It is in this second limit that our colleagues Biasin *et al.* [6] found themselves. While they had insufficient max Q to resolve the fine structure of the molecular

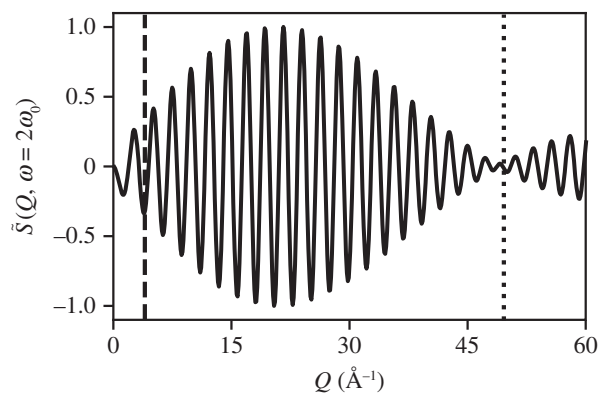


Figure 11. $\tilde{S}(Q, \omega = 2\omega_0)$ generated from $\psi_1(R)\psi_3(R)$ and scaled relative to figure 10. Below 4 \AA^{-1} (dashed line), the $2\omega_0$ signal is no more than 25% of the scattering signal, but is clearly impacted by the amplitude of motion due to a π phase shift relative to the ω_0 signal in figure 10. The node (dotted line) is at $3\pi/A$ for this state.

state directly at the harmonic frequency, their time-resolution of ≈ 30 fs as compared to a period of 330 fs was such that the small amplitude of motion, 0.005 \AA , may have been resolvable as shown.

In conclusion, the above considerations on ω_{\max} and Q_{\max} provide an analogy for the static imaging limit, $d \geq 2\pi/Q_{\max}$. For simple harmonic motion moving with frequency, ω_0 , and amplitude, A , about an equilibrium position, R_0 , $A \geq 2\pi/Q_{\max}$ is the smallest observable amplitude of motion for experiments with $\omega_{\max} \approx \omega_0$. For experiments with $\omega_{\max} \geq \omega_0$, even smaller amplitudes of motion may be observable.

Data accessibility. Access to the full LINAC coherent light source (LCLS) datasets is available upon request. The reduced dataset projected onto Legendre polynomials, $S(Q, \tau) = \sum_l S_l(Q, \tau) P_l(\cos \theta)$, is included as electronic supplementary material. The analysis code is available at [17] with instructions for processing the full or reduced datasets above.

Authors' contributions. M.R.W. carried out the analysis, derived the theory and drafted the manuscript; J.M.G. designed and carried out the experiment and drafted the manuscript; A.N. did initial analysis during beamtime and reviewed the manuscript; J.P.C. helped carry out the experiment, provided initial insight for analysis and reviewed the manuscript; P.H.B. advised the project through experiment and analysis and drafted the manuscript.

Competing interests. There are no competing interests.

Funding. This research is supported through the Stanford PULSE Institute, SLAC National Accelerator Laboratory by the U.S. Department of Energy, Office of Basic Energy Sciences, Atomic, Molecular, and Optical Science Program. Use of the LCLS, SLAC National Accelerator Laboratory, is supported by the U.S. Department of Energy, Office of Basic Energy Sciences under Contract No. DE-AC02-76SF00515.

Acknowledgements. We would like to thank Noor Al-Sayyad for her help commenting the code database in preparation for publication.

Appendix A. Experimental detail

The experimental data were recorded at the LCLS at the X-Ray Pump Probe (XPP) end station [18] with an experimental setup that has already been described in detail elsewhere [4,5,7], and is shown diagrammatically in figure 2. An 800 nm optical laser with a pulse length of 70 fs, a bandwidth of 28 nm FWHM, and a focal intensity of $>10^{13} \text{ W cm}^{-2}$ was focused into a gas cell containing 100°C iodine (50 torr, [19]). The gas cell had a holey mirror to collinearly combine the laser with 9 keV, 40 fs, 2 mJ, $30 \mu\text{m}$ FWHM X-rays from the LCLS. The forward scattered X-rays had a usable angular range of $23\text{--}58.2^\circ$ [4] which corresponds to a Q -range of $1.81\text{--}4.43 \text{ \AA}^{-1}$ as shown in figure 3. The scattered photons were detected using the large area Cornell Stanford Pixel Area Detector (CSPAD) [18] located behind the cell. The XPP beamline's optical/X-ray cross

correlator was used to get timing jitter below 15 fs root-mean-squared [20]. The optical pump delay was varied with respect to the X-rays using an encoded continuously moving translation stage moving delay back and forth between -0.5 ps and 2 ps delay to help average over slow fluctuations in experimental parameters such as beam pointing, position, X-ray intensity, etc.

The high intensity 800 nm laser was likely able to multi-photon ionize some of the iodine, and near t_0 in the observed TRXS shown in figure 5, there is indication of the subsequent rapid dissociation in excess of 30 \AA ps^{-1} , see [7,21] for representative images of strong dissociation in TRXS). The estimate for the dissociation velocity arises from examination of the sloped line in figure 6, where the velocity should go as $v = \Delta\omega/\Delta Q$. Some of the iodine were observed to undergo Raman transitions to higher lying vibrational states. The periodic motion in the observed X-ray scattering pattern is centred about the mean ground state iodine separation of $R_0 = 2.666 \text{ \AA}$ and oscillates with a period of 155.9 ± 3.9 fs as demonstrated in figures 6 and 7. These observations are consistent with previous experiments which have measured an equilibrium separation of 2.666 \AA and a harmonic period of 155.5 fs [11–13].

Appendix B. General theory of time-resolved X-ray scattering from homonuclear diatomics

In the limit of impulsive scattering, the time-dependent X-ray scattering intensity may be expressed as

$$\frac{dI}{d\Omega} = \frac{d\sigma_{Th}}{d\Omega} \int dk I(k) \frac{\omega}{\omega_s} \langle \psi(\tau) | \hat{F}(\mathbf{Q}) | \psi(\tau) \rangle, \quad (\text{B1})$$

where $d\sigma_{Th}/d\Omega$ is the Thomson scattering cross-section, $I(k)$ is the incident X-ray flux, $|\psi(\tau)\rangle$ is the state of the molecule at pump-probe delay $\tau = t - t_0$, k is the incident X-ray momentum, k_s is the scattered X-ray momentum, $\mathbf{Q} = k - k_s$ is the momentum transfer and $\hat{F}(\mathbf{Q}) = \sum_{j,l} e^{i\mathbf{Q}\cdot(\mathbf{r}_j - \mathbf{r}_l)}$ is the scattering operator, where $\mathbf{r}_{j,l}$ are the electronic coordinates [22].

For scattering within the pulse bandwidth ($\omega \approx \omega_s$) and collimated beam input I_0 , equation (B1) reduces to the product of three factors:

$$\frac{dI}{d\Omega} = \frac{d\sigma_{Th}}{d\Omega} I_0 \langle F(\mathbf{Q}, \tau) \rangle, \quad (\text{B2})$$

where $\langle F(\mathbf{Q}, \tau) \rangle$ is a time- and angle-dependent polarization-corrected scattering probability. $\langle F(\mathbf{Q}, \tau) \rangle$ may subsequently be expressed as an incoherent sum of the scattering from each electronic state because the coherent cross-terms between electronic states in X-ray scattering are smaller than the incoherent contributions by several orders of magnitude (e.g. [23]). The incoherent contribution $\langle F_N(\mathbf{Q}, \tau) \rangle$ from each electronic state N is simplified considerably by the independent atom approximation so that the scattering probability for a homonuclear diatomic molecule becomes a simple function of the atomic separation \mathbf{R} [24]:

$$\langle F_N(\mathbf{Q}, \tau) \rangle = 2|f_A(\mathbf{Q})|^2 \left(1 + \text{Re} \left\{ \int d\mathbf{R} \rho_N(\mathbf{R}, \tau) e^{i\mathbf{Q}\cdot\mathbf{R}} \right\} \right). \quad (\text{B3})$$

Here $f_A(\mathbf{Q})$ is the atomic scattering factor and $\rho_N(\mathbf{R}, \tau)$ is the ensemble-averaged nuclear probability density of electronic state N at pump-probe delay τ . The exponential function in equation (B3) can be rewritten using the spherical Bessel expansion:

$$e^{i\mathbf{Q}\cdot\mathbf{R}} = \sum_l i^l (2l+1) P_l(\cos\theta) j_l(QR), \quad (\text{B4})$$

where $j_l(QR)$ is the l th spherical Bessel function. The X-ray diffraction pattern projects onto Legendre polynomials that describe the target probability density [9,25]. For inversion-symmetric systems, e.g. the nuclear probability density following a dipole excitation, only *even* Legendre

polynomials contribute:

$$S_N(Q, \theta, \tau) = \sum_{l=0,2,\dots} \sqrt{\frac{2\pi}{2l+1}} P_l(\cos \theta) S_{N,l}(Q, \tau). \quad (\text{B5})$$

Only the isotropic contribution is considered in this manuscript as given by

$$F_{N,0}(Q, \tau) = 2 |f_A(Q)|^2 \left(1 + \int dR R^2 \text{sinc}(QR) \rho_N(R, \tau) \right). \quad (\text{B6})$$

In particular, the molecular scattering factor is discussed,

$$S_{N,0}(Q, \tau) = \frac{F_{N,0}}{2 |f_A(Q)|^2} - 1 = \int dR R^2 \text{sinc}(QR) \rho_N(R, \tau). \quad (\text{B7})$$

The subscripts have been dropped in the manuscript such that

$$S(Q, \tau) = \int dR R^2 \text{sinc}(QR) \rho(R, \tau) \quad (\text{B8})$$

is written for brevity.

To analyse the experimental data, these theoretical considerations are applied. The measured time-dependent X-ray scattering intensity on the CSPAD, $I(x, y, \tau)$, is used to generate the molecular scattering factor up to a scaling factor and DC offset via

$$F(x, y, \tau) = \frac{I(x, y, \tau)}{(d\sigma_{Th}/d\Omega)(x, y)} \quad (\text{B9})$$

and

$$S(x, y, \tau) = \frac{F(x, y, \tau)}{2 |f_l(x, y)|^2}. \quad (\text{B10})$$

The isotropic component of $S(x, y, \tau)$ as given by $S(Q, \tau)$ is obtained by angularly integrating the data at fixed $Q = 2k_0 \sin \gamma/2$ with respect to the angle, θ , about the laser polarization axis, \hat{e}_y . (These angles are depicted in figure 3.) The angular integration is done by projecting the data onto the zeroth-order Legendre function, i.e. $P_0(\cos \theta) = 1$.

Appendix C. Error propagation

For each shot, the pump-probe delay, τ'_i , is measured and then binned into some time bin, $\tau_j \pm \Delta\tau$. This allows the generation of the mean molecular scattering pattern

$$S(x, y, \tau_j) = \frac{1}{N_j} \sum_i S(x, y, \tau'_i), \quad (\text{C1})$$

where (x, y) indicates each pixel on the CSPAD detector. The variation at each pixel position is generated by

$$\sigma^2(x, y, \tau_j) = \text{Var}(S(x, y, \tau_j)) = \frac{1}{N_j} \sum_i |S(x, y, \tau'_i) - S(x, y, \tau_j)|^2. \quad (\text{C2})$$

The variation is then propagated through the analysis as follows.

For both the isotropic projection of $S(x, y, \tau)$ onto $S(Q, \tau)$ and the temporal Fourier transform of $S(Q, \tau)$ onto $\tilde{S}(Q, \omega)$, a χ^2 -minimization is used. To perform the transforms

$$\chi^2 = \sum_l \frac{(p_l - s_l)^2}{\sigma_l^2}, \quad (\text{C3})$$

is minimized, where p_l is the fitted function, s_l is the data, and σ_l^2 is the variance. For a linear model, the fitted function may be expressed as $p_l = \sum_j x_j f_j(Q_l)$, where x_j are the model coefficients.

Then the solution to the χ^2 -minimization is

$$x_k = \sum_i \frac{A_{ki}s_i}{\sigma_i^2}, \quad (\text{C } 4)$$

where $A = (f^T \sigma^{-2} f)^{-1} f$. The associated error for the solution, x_k , is then

$$\sigma_k \leq \sum_j |A_{kj} \sigma_j^{-1}|, \quad (\text{C } 5)$$

as shown in [26].

For the isotropic projection of $S(x, y, \tau)$ onto $S(Q, \tau)$, the fitted function is $f_j(\theta_i) = P_j(\cos \theta_i)$, where $j = 0, 2, 4$ are used to find a reduced χ^2 of about 1. The obtained result is $x_j(Q, \tau) = S_j(Q, \tau)$, where $j = 0$ is the desired isotropic contribution, denoted $\tilde{S}(Q, \omega)$ in the main text.

For the temporal Fourier transform of $S(Q, \tau)$ into $\tilde{S}(Q, \omega)$, the fitted function is $f_j(\tau_i) = \cos(\omega_j \tau_i)$, where $\omega_j \in (0, \pi/\Delta\tau)$ and $\Delta\tau = 30$ fs was used in this analysis.

References

- Bredtmann T, Ivanov M, Dixit G. 2014 X-ray imaging of chemically active valence electrons during a pericyclic reaction. *Nat. Commun.* **5**, 5589. (doi:10.1038/ncomms6589)
- Ben-Nun M, Cao J, Wilson KR. 1997 Ultrafast x-ray and electron diffraction: theoretical considerations. *J. Phys. Chem. A* **101**, 8743–8761. (doi:10.1021/jp971764c)
- Cao J, Wilson KR. 1998 Ultrafast x-ray diffraction theory. *J. Phys. Chem. A* **102**, 9523–9530. (doi:10.1021/jp982054p)
- Budarz JM, Minitti MP, Cofer-Shabica DV, Stankus B, Kirrander A, Hastings JB, Weber PM. 2016 Observation of femtosecond molecular dynamics via pump-probe gas phase x-ray scattering. *J. Phys. B: At. Mol. Opt. Phys.* **49**, 034001. (doi:10.1088/0953-4075/49/3/034001)
- Minitti MP *et al.* 2015 Imaging molecular motion: femtosecond x-ray scattering of an electrocyclic chemical reaction. *Phys. Rev. Lett.* **114**, 255501. (doi:10.1103/PhysRevLett.114.255501)
- Biasin E *et al.* 2016 Femtosecond x-ray scattering study of ultrafast photoinduced structural dynamics in solvated $[\text{Co}(\text{terpy})_2]^{2+}$. *Phys. Rev. Lett.* **117**, 013002. (doi:10.1103/PhysRevLett.117.013002)
- Glownia JM *et al.* 2016 Self-referenced coherent diffraction x-ray movie of Ångstrom- and femtosecond-scale atomic motion. *Phys. Rev. Lett.* **117**, 153003. (doi:10.1103/PhysRevLett.117.153003)
- Yang J *et al.* 2016 Diffractive imaging of coherent nuclear motion in isolated molecules. *Phys. Rev. Lett.* **117**, 153002. (doi:10.1103/PhysRevLett.117.153002)
- Lorenz U, Møller KB, Henriksen NE. 2010 On the interpretation of time-resolved anisotropic diffraction patterns. *New J. Phys.* **12**, 113022. (doi:10.1088/1367-2630/12/11/113022)
- Kirrander A, Weber PM. 2017 Fundamental limits on spatial resolution in ultrafast x-ray diffraction. *Appl. Sci.* **7**, 534. (doi:10.3390/app7060534)
- Wei J, Tellinghuisen J. 1974 Parameterizing diatomic spectra: 'Best' spectroscopic constants for the $I_2 B \leftrightarrow X$ transition. *J. Mol. Spectrosc.* **50**, 317–332. (doi:10.1016/0022-2852(74)90239-2)
- Barrow RF, Yee KK. 1973 $B^3\Pi_{0+u} - X^1\Sigma_g^+$ system of $^{127}I_2$: rotational analysis and long-range potential in the $B^3\Pi_{0+u}$ state. *J. Chem. Soc. Faraday Trans. 2: Mol. Chem. Phys.* **69**, 684–700. (doi:10.1039/F29736900684)
- LeRoy RJ. 1970 Molecular constants and internuclear potential of ground-state molecular iodine. *J. Chem. Phys.* **52**, 2683–2689. (doi:10.1063/1.1673358)
- Jonas DM, Bradforth SE, Passino SA, Fleming GR. 1994 Ground state wavepackets in pump-probe spectroscopy. In *Proc. of the Royal Netherlands Academy Colloquium on Femtosecond Reaction Dynamics*, pp. 133–145. Amsterdam, The Netherlands: North Holland.
- Hollas JM. 2004 *Modern spectroscopy*. New York, NY: John Wiley & Sons.
- Als-Nielsen J, McMorrow D. 2011 *Elements of modern X-ray physics*, 2nd edn. Hoboken, NJ: Wiley.
- Ware MR. Code base. See <https://github.com/mrware91/PhilTransA-TRXS-Limits>.

18. Chollet M *et al.* 2015 The X-ray pump–probe instrument at the linac coherent light source. *J. Synchrotron Radiat.* **22**, 503–507. (doi:10.1107/S1600577515005135)
19. Baxter GP, Hickey CH, Holmes WC. 1907 The vapor pressure of iodine. *J. Am. Chem. Soc.* **29**, 127–136. (doi:10.1021/ja01956a004)
20. Harmand M *et al.* 2013 Achieving few-femtosecond time-sorting at hard X-ray free-electron lasers. *Nat. Photonics* **7**, 215–218. (doi:10.1038/nphoton.2013.11)
21. Debnarova A, Techert S, Schmatz S. 2010 Ab initio studies of ultrafast x-ray scattering of the photodissociation of iodine. *J. Chem. Phys.* **133**, 124309. (doi:10.1063/1.3475567)
22. Hau-Riege SP. 2015 *X-ray scattering*, pp. 235–264. Wiley-VCH. See <http://onlinelibrary.wiley.com/stanford.idm.oclc.org/doi/10.1002/9783527664498.ch16/summary>.
23. Kowalewski M, Bennett K, Mukamel S. 2017 Monitoring nonadiabatic avoided crossing dynamics in molecules by ultrafast X-ray diffraction. *Struct. Dyn.* **4**, 054101. (doi:10.1063/1.4984241)
24. Henriksen NE, Møller KB. 2008 On the theory of time-resolved x-ray diffraction. *J. Phys. Chem. B* **112**, 558–567. (doi:10.1021/jp075497e)
25. Baskin JS, Zewail AH. 2006 Oriented ensembles in ultrafast electron diffraction. *ChemPhysChem* **7**, 1562–1574. (doi:10.1002/cphc.v7:7)
26. Taylor J. 1997 *Introduction to error analysis, the study of uncertainties in physical measurements*. Sausalito, CA: University Science Books.